

# Supramolecular Modulation of Hybrid Perovskite Solar Cells via Bifunctional Halogen Bonding Revealed by Two-Dimensional $^{19}\text{F}$ Solid-State NMR Spectroscopy

Marco A. Ruiz-Preciado,<sup>†,‡</sup> Dominik J. Kubicki,<sup>†,‡,∇,#</sup> Albert Hofstetter,<sup>‡,#</sup> Lucie McGovern,<sup>§</sup> Moritz H. Futscher,<sup>§</sup> Amita Ummadisingu,<sup>†,∇</sup> Renana Gershoni-Poranne,<sup>||</sup> Shaik M. Zakeeruddin,<sup>†</sup> Bruno Ehrler,<sup>§</sup> Lyndon Emsley,<sup>\*,‡</sup> Jovana V. Milić,<sup>\*,†</sup> and Michael Grätzel<sup>\*,†</sup>

<sup>†</sup>Laboratory of Photonics and Interfaces, École Polytechnique Fédérale de Lausanne, Lausanne 1015, Switzerland

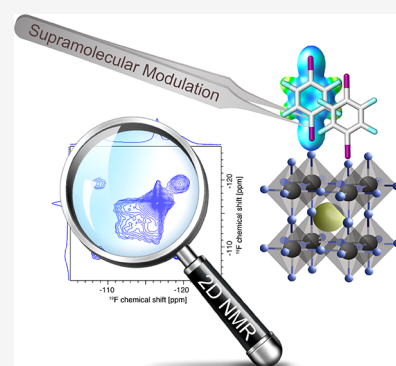
<sup>‡</sup>Laboratory of Magnetic Resonance, École Polytechnique Fédérale de Lausanne, Lausanne 1015, Switzerland

<sup>§</sup>Center for Nanophotonics, AMOLF, Amsterdam 1009 DB, The Netherlands

<sup>||</sup>Laboratory of Organic Chemistry, ETH Zurich, Zurich 8093, Switzerland

## Supporting Information

**ABSTRACT:** There has been an ongoing effort to overcome the limitations associated with the stability of hybrid organic–inorganic perovskite solar cells by using different organic agents as additives to the perovskite formulations. The functionality of organic additives has been predominantly limited to exploiting hydrogen-bonding interactions, while the relevant atomic-level binding modes remain elusive. Herein, we introduce a bifunctional supramolecular modulator, 1,2,4,5-tetrafluoro-3,6-diiodobenzene, which interacts with the surface of the triple-cation double-halide perovskite material via halogen bonding. We elucidate its binding mode using two-dimensional solid-state  $^{19}\text{F}$  NMR spectroscopy in conjunction with density functional theory calculations. As a result, we demonstrate a stability enhancement of the perovskite solar cells upon supramolecular modulation, without compromising the photovoltaic performances.



## INTRODUCTION

Over the past decade, hybrid perovskite solar cells have achieved extraordinary success, demonstrating solar-to-electric power conversion efficiencies exceeding 25% and surpassing the performance of polycrystalline silicon.<sup>1–3</sup> The structure of the corresponding light absorber, hybrid organic–inorganic perovskites, can be defined by the  $\text{AMX}_3$  formula, which represents a three-dimensional (3D) perovskite structure (Figure 1a). In a typical perovskite composition, A cations can be organic (e.g., methylammonium (MA), formamidinium (FA)) or inorganic (e.g.,  $\text{Cs}^+$ ), M are divalent metal cations (mainly  $\text{Pb}^{2+}$  or  $\text{Sn}^{2+}$ ), and X are halide anions ( $\text{I}^-$ ,  $\text{Br}^-$ ,  $\text{Cl}^-$ ).<sup>1–3</sup> Despite its remarkable performance, the progress of this thin-film photovoltaic technology is limited by the material stability, particularly with respect to the reactivity to light, oxygen, and water as well as the internal ion migration under the device operation conditions.<sup>4</sup>

Various strategies have been used to overcome this challenge, such as employing different organic molecules as additives to the perovskite composition as well as use of hydrophobic agents to treat (i.e., *passivate*; Figure 1b) the surface of the perovskite material.<sup>1,5</sup> However, there are several shortcomings associated with this widely employed approach. First, many organic agents provide stabilization at the expense of performance by stabilizing the devices at lower power

conversion efficiencies,<sup>6,7</sup> and overcoming this requires advanced function-driven molecular design. Furthermore, most of the research effort is based on the trial-and-error approach and predominantly exploits ammonium-functionalized organic molecules that are assumed to form hydrogen bonds with the perovskite surface, thereby mimicking the native A-site cation.<sup>1</sup> In this context, bifunctional organic systems are gaining increasing interest due to their potential to *crosslink* perovskite grains (Figure 1c), which is beneficial for the performance,<sup>8,9</sup> although the crosslinking role of the organic components is seldom identified at the atomic level. Bifunctional systems also favor the formation of layered two-dimensional (2D) structures with superior environmental stability.<sup>10–12</sup> There are, however, very few examples of using alternative noncovalent interactions, such as halogen bonding,<sup>13,14</sup> despite its immense potential.<sup>15–18</sup> Until now, the corresponding device performance has been the overarching focus of these studies, while structure–property relationships and the underlying modes of interaction remain poorly understood, thus limiting the prospects of advanced molecular-level design.<sup>19</sup>

Received: December 19, 2019

Published: January 8, 2020

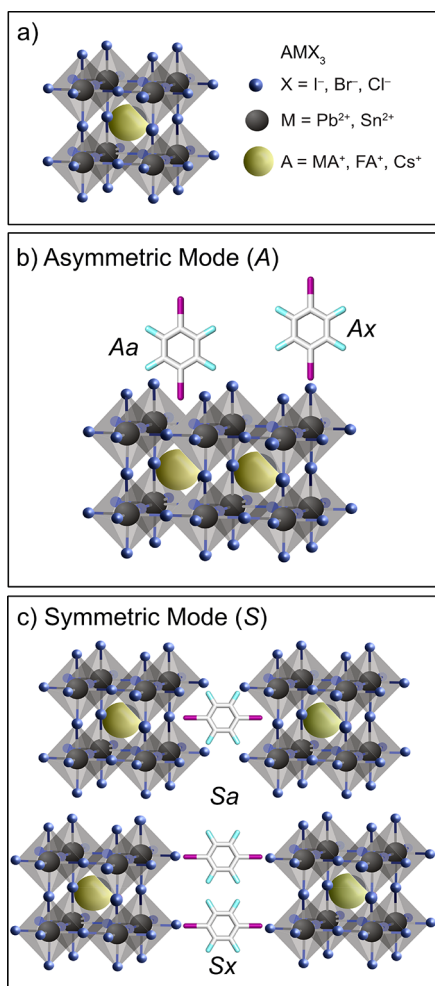


**Figure 1.** (a) The structure of hybrid perovskites ( $AMX_3$ ). Schematic representation of different binding modes of the prospective molecular modulator to the perovskite, that is, (b) *asymmetric* interaction (A) and (c) *symmetric* crosslinking of the phases (S), both of which feature two distinct binding sites, either the A-cation vacancy (Aa/Sa) or halogen anions (Ax/Sx).

We recently demonstrated that solid-state NMR spectroscopy is a powerful tool for unraveling the atomic-level interactions of molecularly engineered organic molecules with hybrid perovskites.<sup>19</sup> While these *molecular modulators* encompassed multiple functional groups with complementary roles and their interactions with the perovskite surface (e.g., through hydrogen bonding), as well as  $PbI_2$  (e.g., via metal coordination), were evidenced, the different binding modes within the perovskite framework could not be distinguished by conventional one-dimensional (1D) NMR spectroscopy (Figure 1b,c). Moreover, these modulators have been based on conventional hydrogen bonding (HB) and metal-coordination, whereas the role of halogen bonding (XB) interactions remains poorly understood. In this regard, a more versatile tool is required, and we recently showed that the 2D spin diffusion (SD) NMR spectroscopy can be effectively employed to scrutinize the structure of layered hybrid perovskites.<sup>11</sup> This unique diagnostic tool could provide the atomic-level understanding necessary to extend the impact of modulation on the perovskite solar cell performance and stability, such as by exploiting alternative noncovalent interactions.

Herein, we demonstrate the effect of a bifunctional modulator, 1,2,4,5-tetrafluoro-3,6-diiodobenzene (TFDIB), which uniquely interacts with hybrid perovskites via XB. We unravel its mode of action by using 2D  $^{19}F$  solid-state NMR spectroscopy as an unambiguous diagnostic tool in conjunction with density functional theory (DFT) calculations. Modulation of the perovskite solar cells results in improved stability under continuous illumination, while the competitive photovoltaic performance is maintained. This showcases the potential of supramolecular modulation via XB in solar cell research. Our work unravels the role of bifunctional XB in improving perovskite solar cell stability and structure–property relationships for advanced molecular design in hybrid perovskite optoelectronics.

## EXPERIMENTAL DETAILS

**Material Synthesis.** Material synthesis involved the perovskite precursor solution (1.4 M) that was prepared by dissolving the corresponding proportion of lead iodide ( $PbI_2$ , 99.99%, TCI), lead bromide ( $PbBr_2$ , 99.99%, TCI), cesium iodide (CsI, 99.998%, ABCR), methylammonium bromide (MABr, 98%, Greatcellsolar) and formamidinium iodide (FAI,  $\geq 98\%$ , Greatcellsolar) in dimethylformamide (DMF, 99.8%, Acros) and dimethyl sulfoxide (DMSO, 99.7%, Acros) (DMF:DMSO = 4:1 v/v) to form a triplecation perovskite containing 5% Cs and 10% MA, 10% Br, and 3% excess of  $PbI_2$ . The perovskite precursor solution was prepared in an argon-filled glovebox.

**Thin-Film Preparation.** Thin films were prepared by spin-coating the perovskite precursor solution on the defined substrates. The perovskite precursor solution was drop-casted on the substrates and spun at 2000 rpm (acceleration of 200 rpm  $s^{-1}$ ) and 6000 rpm (acceleration of 2000 rpm  $s^{-1}$ ) for 10 and 30 s, respectively. During the last 10 s of the second spin-coating step, 220  $\mu L$  of the  $\alpha,\alpha,\alpha$ -trifluorotoluene antisolvent (TFT, 99%, anhydrous, Sigma-Aldrich) was drop-casted. The perovskite film was then dried on a hot plate at 100  $^{\circ}C$  for 60 min to form a ca. 450 nm-thick perovskite layer.

**Molecular Modulation of Thin Films.** Molecular modulation of thin films was performed by using the corresponding modulator (TFDIB) in one of the following three ways, which are specified throughout the manuscript, namely: (1) as part of the perovskite precursor solution, (2) by treating the perovskite surface using the solution of the modulator in isopropanol, or (3) by using the modulator within the antisolvent (TFT) in specified concentrations.

**Mechanosynthesis.** Samples for the NMR experiments were prepared using mechanochemistry<sup>20–22</sup> by grinding the reactants in an electric ball mill (Retsch Ball Mill MM-200) using a grinding jar (10 mL) and a ball ( $\varnothing 10$  mm) for 30 min at 25 Hz. The following stoichiometries were used: m- $PbI_2$ :  $PbI_2$  (461 mg, 1 mmol), TFDIB (40 mg, 0.1 mmol); m-MAI: MAI (159 mg, 1 mmol), TFDIB (20 mg, 0.05 mmol); m-MAPbI<sub>3</sub>: MAI (159 mg, 1 mmol),  $PbI_2$  (461 mg, 1 mmol), TFDIB (20 mg, 0.05 mmol); m-FAPbI<sub>3</sub>: FAI (172 mg, 1 mmol),  $PbI_2$  (461 mg, 1 mmol), TFDIB (20 mg, 0.05 mmol). The powders were packed into 3.2 mm zirconia rotors and annealed at 140  $^{\circ}C$  for 5 min to remove grinding-induced defects and transferred into the probe. The measurements were carried out under dry nitrogen.

**Solid-State NMR Experiments.** NMR experiments were carried out on a 9.4 T magnet equipped with a Bruker Advance III console using a 3.2 mm LTMAS probe. Echo-detected  $^{19}F$  and  $^{19}F$ – $^{19}F$  spin-diffusion magic angle spinning (MAS) NMR spectra were recorded using 100 kHz RF strength and no  $^1H$  decoupling. Relaxation delays between 5 and 60 s were used.  $^{19}F$  chemical shifts were referenced to neat  $CFCl_3$  (0 ppm) using solid NaF as a secondary reference ( $-224$  ppm). Further experimental details (number of scans, recycle delays, etc.) are summarized in the Supporting Information (Table S2, SI). We note that the probe background does not contribute appreciably to the detected signals (Figure S2, SI).

**Device Fabrication.** Photovoltaic devices were fabricated using the n–i–p architecture with the constituent layers as follows: FTO/(40 nm) c-TiO<sub>2</sub>/(250 nm) mp-TiO<sub>2</sub>/(450 nm) perovskite/(180 nm) Spiro-OMeTAD/(80 nm) Au. An active area of 0.25 cm<sup>2</sup> (5 mm × 5 mm) was defined by the gold electrodes, and a 0.16 cm<sup>2</sup> black metal mask was used during PV measurements to define the aperture area. For this purpose, glass sheets covered by fluorine-doped tin oxide (Nippon sheet glass 8 Ω·sq<sup>-1</sup>) were thoroughly brushed with a 10% Hellmanex (Hellma GmbH) water solution and then placed under sonication in a 2% Hellmanex water solution for 30 min. After that, the Hellmanex solution was replaced by acetone and later ethanol and sonicated during 15 and 10 min, respectively. Then, a ca. 40 nm-thick TiO<sub>2</sub> compact layer (c-TiO<sub>2</sub>) was deposited by spray pyrolysis with a precursor solution of titanium diisopropoxide bis(acetylacetonate) (75 wt % in isopropanol, Sigma-Aldrich) in anhydrous ethanol (99.5%, Fischer Scientific) at 450 °C. After the spraying, the substrates were kept at 450 °C for 30 min. Then, a suspension of TiO<sub>2</sub> paste (Dyesol 30 NR-D) in ethanol was used to cast a ca. 250 nm-thick mesoporous TiO<sub>2</sub> (mp-TiO<sub>2</sub>) layer by spin coating at 4000 rpm for 20 s with an acceleration of 2000 rpm s<sup>-1</sup>. After the spin coating, the solvent was allowed to evaporate on a hot plate at 80 °C for 10 min and then sintered at 450 °C for 30 min under dry air flow. UV-ozone treatment for 15 min was used before the deposition of the c-TiO<sub>2</sub> and mp-TiO<sub>2</sub> layers. A ca. 450 nm-thick perovskite layer was deposited on the substrates by spin coating following the antisolvent method. The precursor perovskite solution was drop-casted on the substrates and spun at 2000 rpm (acceleration of 200 rpm s<sup>-1</sup>) and 6000 rpm (acceleration of 2000 rpm s<sup>-1</sup>) for 10 and 30 s, respectively. During the last 10 s of the second spin-coating step, 220 μL of the TFT (99%, anhydrous, Sigma-Aldrich) was drop-casted. The perovskite film was then dried on a hot plate at 100 °C for 60 min. The substrates were allowed to cool down for 10 min. A 70 mM solution of Spiro-OMeTAD (99%, Merck) in chlorobenzene (CB, 99.8%, ACROS) was prepared. Lithium bis(trifluoro-methylsulfonyl)imide (Li-TFSI, 99.95%, Sigma) and 4-*tert*-butylpyridine (4-tBP, 96%, Sigma-Aldrich) were used as additives in a 0.5 and 3.3 mol % (relative to Spiro-OMeTAD), respectively. This solution was spin-coated on the perovskite layer at 2000 rpm (acceleration of 1200 rpm s<sup>-1</sup>) for 20 s to form a ca. 180 nm hole-transporting layer. The perovskite and Spiro-OMeTAD layers were deposited in a dry air glovebox. Finally, 80 nm-thick gold electrodes were deposited by thermal evaporation.

**Transient Capacitance Measurements.** Ionic motion was analyzed by carrying out the temperature-dependent transient capacitance measurements in accordance with the previously reported procedures,<sup>23</sup> which are further detailed in the Supporting Information.

**Other Experimental Details.** More details are provided in the corresponding sections of the Supporting Information.

## ■ SUPRAMOLECULAR DESIGN

It has been shown that organic molecules featuring strong hydrogen bond donors, typically ammonium (NH<sub>3</sub><sup>+</sup>) groups, have the capacity to interact with the A-cation vacancies on the surface of hybrid perovskites through HB.<sup>1,19,25,26</sup> This can lead to morphology alteration, passivation of anionic defects (e.g., halide ions), or increase in stability by inducing resilience toward moisture and oxygen.<sup>1</sup> These effects can be amplified by employing systems featuring multiple functional groups that may, for instance, crosslink perovskite grains (Figure 1c)<sup>9</sup> or simultaneously interact with the perovskite surface while passivating perovskite defects.<sup>19</sup> These effects can be achieved by effectively employing alternative noncovalent interactions, such as XB.<sup>17</sup> Unlike HB, XB requires a halogen bond donor, which is a highly polarized halogen atom (X), and a nucleophilic halogen bond acceptor, such as N, O, or another halogen. The XB interaction takes place through an area of positive potential along the C–X bond axis known as the  $\sigma$

hole, which renders XB highly directional (Figure 2a).<sup>27–29</sup> Since the strength of XB is determined by the orientation of the participating groups and the size of the  $\sigma$  hole, it can be enhanced by employing strong electron-withdrawing groups as carriers of the XB donor atom, which should be highly polarizable.<sup>15–17</sup> In addition to these requirements associated with XB, a suitable supramolecular agent for stabilizing the perovskite should also feature increased hydrophobicity, ensuring resilience against environmental factors.<sup>5</sup> TFDIB is a bifunctional halogen-bond-donating molecule that meets these design criteria, while incorporating them into a perfluorinated  $\pi$  system with pronounced hydrophobicity (Figure 2). We assessed the capacity of TFDIB to act as a supramolecular XB modulator with scanning electron microscopy (SEM), UV–vis absorption and photoluminescence (PL) spectroscopy, and X-ray diffraction, complemented by NMR spectroscopy.

**Effect of XB on Hybrid Perovskite Material Properties.** To assess the effect of XB on the perovskite, thin films of (FA<sub>0.9</sub>MA<sub>0.1</sub>)<sub>0.95</sub>Cs<sub>0.05</sub>Pb<sub>1.03</sub>(I<sub>0.93</sub>Br<sub>0.1</sub>)<sub>3</sub> were deposited onto microscope glass slides using a two-step spin-coating (for details see the Experimental Details and Supporting Information, SI). The XB modulating layer was cast over the perovskite layer by spin-coating a solution containing TFDIB in a highly hydrophobic solvent, namely TFT, used to induce perovskite film crystallization (i.e., antisolvent).<sup>30</sup> The solution was spun at a velocity of 4000 rpm for 20 s with an acceleration of 2000 rpm s<sup>-1</sup> followed by annealing at 100 °C for 10 min.

The surface morphology of pristine and XB-modulated perovskite films was analyzed by SEM. Top-view SEM images reveal a comparable grain size of the pristine and modulated samples (Figure 3a). Furthermore, the X-ray diffraction (XRD) patterns of thin films suggest that the XB-modulating layer does not lead to substantial structural changes, as the characteristic angle reflections remain unaltered (Figure 3b). Similarly, the optical properties were not significantly altered, as demonstrated by the UV–vis absorption spectroscopy and PL spectra of the films (Figure 4). Tauc analysis of the absorption spectra reveals a band gap of ~1.59 eV for both pristine and XB-modulated films (Figure 4a, inset). This value correlates very well with the PL emission peak (~1.59 eV;

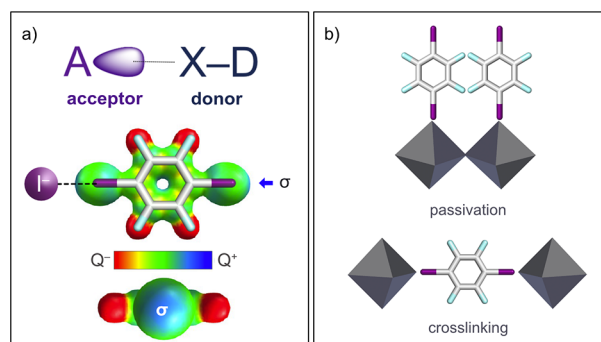


**Figure 2.** (a) Upper: Schematic representation of XB between an XB acceptor (A) and donor (X). Lower: The structure and optimized geometry (DFT calculations at the B3LYP/def2tzvp level of theory)<sup>24</sup> of TFDIB, with the corresponding top and side views of the electrostatic potential surface highlighting the  $\sigma$ -hole.<sup>17</sup> (b) Envisaged modes of interaction of TFDIB with the hybrid perovskite: asymmetric surface passivation (top) and symmetric crosslinking (bottom) of the perovskite grains.

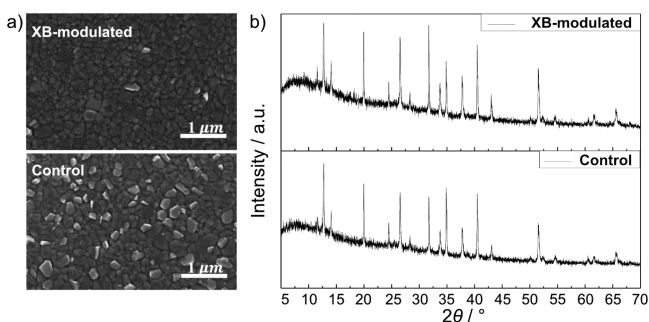


**Figure 3.** Morphology and structural properties of the perovskite thin films. (a) Top-view SEM images and (b) XRD patterns of pristine (control) and XB-modulated perovskite films on FTO/c-TiO<sub>2</sub>/mp-TiO<sub>2</sub>. No signals were observed at  $2\theta < 10^\circ$ . FTO = fluorine doped tin oxide; c = compact; mp = mesoporous.

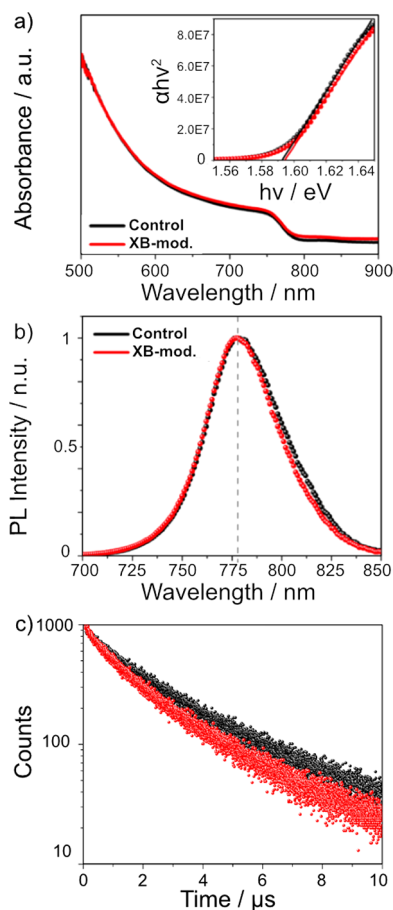


**Figure 4.** Optoelectronic properties of pristine (control, black) and XB-modulated (mod.; red) perovskite films. (a) UV-vis absorption spectra and (b) steady-state PL spectra.  $\tau_{\text{auc}}$  plots are shown in the inset. (c) Time-resolved PL trace upon excitation at 420 nm and detection at 790 nm. The corresponding fitted PL curves (Figure S1) and parameters (Table S1) are shown in the SI.

Figure 4b). The close match between the band gap extracted from optical absorption and the PL emission peak indicates that the latter originates from band-to-band recombination. We can thus conclude that the optoelectronic properties of the material are not substantially affected by XB. This observation, however, does not exclude possible effects on the conductivities of the materials. For more insight into the electronic quality of the perovskite films, time-resolved PL measurements

were performed to assess the photogenerated charge carrier dynamics.<sup>31–34</sup> An exponential function was fitted to the decay traces measured on a control perovskite film and a XB-modulated film deposited on a glass microscope slide (Figure 4c; see SI for details) to estimate the PL decay time. The decay time was found to be similar for both the control (1.57  $\mu\text{s}$ ) and modulated (1.53  $\mu\text{s}$ ) samples (Table S1, SI). The analysis of the decay profiles estimates lifetimes on the order of  $\mu\text{s}$ , which indicates high electronic quality of the perovskite films that is preserved in the presence of the modulator.

In summary, the analysis of the effects of XB modulation on the properties of the perovskite suggests the modulation does not affect the electronic quality of the perovskite films. Since the XRD patterns of the films did not reveal substantial changes in the long-range crystalline order, the short-range local structure of the modulated hybrid perovskite materials was further investigated by solid-state NMR spectroscopy.<sup>35–39</sup>

**Local Structure of XB-Modulated Perovskites.** To assess the atomic-level structure of the XB-modulated perovskites, we recorded powder XRD (PXRD; Figure S1, SI), <sup>19</sup>F echo-detected (Figure 5a–e) and <sup>19</sup>F–<sup>19</sup>F spin-diffusion (SD; Figure 5f–i) magic angle spinning (MAS) NMR spectra of modulated materials prepared by solid-state mechanochemistry. XRD patterns of the corresponding perovskite powders do not reveal any substantial changes upon modulation for various perovskite compositions (Figure S1, SI). However, we observe presence of a nonperovskite  $\delta$ -FAPbI<sub>3</sub> phase in the pristine FAPbI<sub>3</sub> material, which was not observed in the modulated (m-) FAPbI<sub>3</sub>, suggesting that the modulator stabilizes the  $\alpha$ -FAPbI<sub>3</sub> perovskite phase under these conditions.<sup>11,36,37</sup>

<sup>19</sup>F–<sup>19</sup>F spin-diffusion measurements yield 2D spectra that are symmetric across the diagonal. The f1 and f2 projections yield the corresponding 1D <sup>19</sup>F spectra, while the cross-peaks arise due to exchange of magnetization through dipole–dipole interaction and therefore provide direct evidence of atomic-level proximity between <sup>19</sup>F environments with different chemical shifts. Neat TFDIB yields two NMR peaks, which can conceivably correspond to either two inequivalent molecules inside a unit cell or two polymorphs (Figure 5a). We thus carried out <sup>19</sup>F–<sup>19</sup>F spin-diffusion (SD) measurements (Figure 5f) to establish if the two species are in close contact, which would be the case for two inequivalent molecules in the unit cell but not for the polymorphs. The two signals exchange magnetization driven by the dipolar coupling rapidly, for mixing times below 5 ms, and therefore correspond to two fluorine environments inside an asymmetric unit cell. The spin–lattice relaxation time is, within the margin of error, identical for both signals ( $T_1 = 14.5$  s), consistent with fast <sup>19</sup>F–<sup>19</sup>F spin diffusion.<sup>39,40</sup>

We subsequently verified the propensity of TFDIB to react with PbI<sub>2</sub> (further referred to as a modulated, m-, sample) (Figure 5b) where TFDIB is present as a modulator at 5–10 mol % concentration, as indicated in the corresponding figure captions. m-PbI<sub>2</sub> yields four new <sup>19</sup>F signals. Down-field shifts (to higher ppm values) of the TFDIB signal were previously observed for XB formed with aromatic N-donors.<sup>39</sup> We therefore deduce that the new chemical environments correspond to halogen-bonded TFDIB. Moreover, <sup>19</sup>F–<sup>19</sup>F SD measurements (Figure 5g) indicate that the signals at –108 and –119 ppm correspond to a species within a single phase (assigned as species 1,  $T_1 = 11.9$  s), and so do the signals at –115 and –116 ppm (species 2,  $T_1 = 0.8$  s). The broad

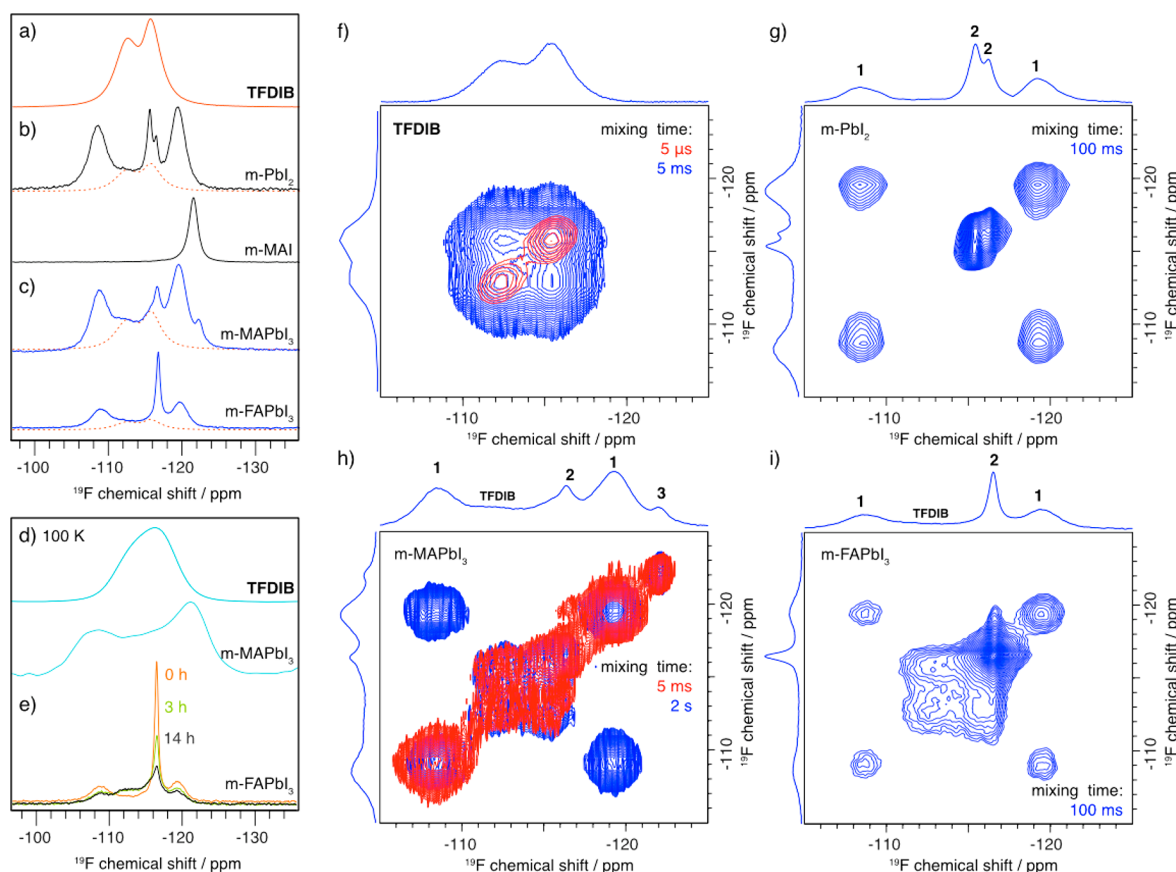


**Figure 5.** Structural properties of XB-modulated perovskite materials.  $^{19}\text{F}$  echo-detected and  $^{19}\text{F}$ – $^{19}\text{F}$  spin-diffusion MAS NMR spectra at 9.4 T and 20 kHz MAS.  $^{19}\text{F}$  echo-detected MAS NMR spectra of (a) neat **TFDIB** and mechanochemical bulk modulated (m-) (b)  $\text{PbI}_2$  and MAI as well as (c)  $\text{MAPbI}_3$  and  $\alpha\text{-FAPbI}_3$  at 298 K. (d)  $^{19}\text{F}$  echo-detected MAS NMR spectra of (d) neat **TFDIB** and mechanochemical bulk m- $\text{MAPbI}_3$  with the (e) evolution of the  $^{19}\text{F}$  echo-detected MAS NMR spectra of m- $\alpha\text{-FAPbI}_3$  at 298 K over time, indicating the dynamic nature of the interaction with the modulator. Modulated (m-) materials contain 5 mol % of the **TFDIB** (10 mol % in the case of m- $\text{PbI}_2$ ).  $^{19}\text{F}$ – $^{19}\text{F}$  spin-diffusion MAS NMR spectra at 9.4 T, 20 kHz MAS, and 298 K of (f) neat **TFDIB**, and mechanochemical bulk modulated (g)  $\text{PbI}_2$ , (h)  $\text{MAPbI}_3$ , and (i)  $\alpha\text{-FAPbI}_3$ . Further experimental details (recycle delays and number of scans) are reported in the SI (Table S2), along with the confirmation that the probe background does not contribute to the detected signals (Figure S2, SI).

overlapping signal corresponds to unreacted **TFDIB** (indicated by a red dashed line in Figure 5b,c), whose presence signals a lack of propensity to form a stoichiometric compound with  $\text{PbI}_2$ ; **TFDIB** rather binds to its surface via weak noncovalent interactions. The interaction of **TFDIB** with  $\text{PbI}_2$  via XB could render the *para*- and *meta*-fluorine substituents magnetically inequivalent and lead to two chemical shifts (Figure 2b, top). Another possible scenario is that of *symmetric* coordination of both iodine atoms to two different  $\text{PbI}_2$  units, in which case the *ortho*- and *meta*-fluorine have comparable or identical chemical shifts, depending on the overall geometry (Figure 2b, bottom). Since two sets of peaks are observed experimentally (assigned as species 1, with a chemical shift difference of 11 ppm, and species 2, with a chemical shift difference of 1 ppm), we tentatively assign species 1 to the *asymmetric* and species 2 to the *symmetric* coordination mode (illustrated schematically in Figure 1b,c and Figure 2b).

Analogous results were obtained for m- $\text{MAPbI}_3$  and m- $\alpha\text{-FAPbI}_3$  (Figure 5c). In m- $\text{MAPbI}_3$ , **TFDIB** also forms species 1 (–108, –119 ppm,  $T_1 = 11.7$  and 8.9 s, respectively) and 2 (–116 ppm,  $T_1 = 0.8$  s). Moreover, an additional product (species 3) is formed (–122 ppm,  $T_1 = 4.2$  s). To assess the origin of this species, we analyzed a mixture of **TFDIB** with MAI, which yields a single peak at –121 ppm, matching the

species present in m- $\text{MAPbI}_3$ . This environment therefore most likely corresponds to the interaction with the ammonium group of MAI, as further confirmed by DFT calculations (for details see Section S2 in the SI). The  $^{19}\text{F}$ – $^{19}\text{F}$  SD spectrum of m- $\text{MAPbI}_3$  (Figure 5h) indicates that, as previously, the two signals of species 1 exchange magnetization and correspond to a fluorine environment within a single phase or molecule. The two peaks of species 1 require mixing times longer than 10 ms to efficiently exchange polarization, suggesting that they correspond to F atoms that are separated by a distance larger than that in the unit cell of pristine **TFDIB**. Species 2 and 3 do not exchange magnetization with any other signals even for very long mixing times (100 ms) and therefore correspond to **TFDIB** molecules that are spatially separated from **TFDIB** molecules in the other binding modes. The sample also contains unreacted **TFDIB** whose peaks exchange polarization within <5 ms of mixing and are thereby correlated with each other in the 2D SD spectrum. The presence of unreacted **TFDIB** strongly indicates that it does not form stoichiometric compounds with the perovskite but rather binds to the limited number of exposed surface sites. The MAI-**TFDIB** adduct (species 3) accounts for only ~4% of the  $^{19}\text{F}$  environments present in this sample, which suggests that the formation of perovskite-bound **TFDIB** species is strongly preferred.

In the modulated  $\alpha$ -FAPbI<sub>3</sub> sample, TFDIB forms only species 1 (−108, −119 ppm,  $T_1$  = 7.3 and 6.5 s, respectively) and 2 (−116 ppm,  $T_1$  = 0.8 s). We have found no evidence for the formation of an analogous FAI-TFDIB in this case. As previously, the <sup>19</sup>F–<sup>19</sup>F SD spectrum (Figure 5i) shows that the two chemical environments of species 1 are coupled and that species 1 and 2 are spatially separated, which is in accordance with their initial assignment to the *asymmetric* and *symmetric* binding modes, respectively.

Finally, low-temperature (100 K) spectra of neat TFDIB and m-MAPbI<sub>3</sub> (Figure 5d) reveal pronounced broadening associated with the freezing of molecular dynamics of TFDIB, leading to static disorder and stronger <sup>19</sup>F–<sup>19</sup>F dipole–dipole couplings. Moreover, in the mixture of TFDIB with  $\alpha$ -FAPbI<sub>3</sub> (Figure 5e), the <sup>19</sup>F spectrum at 298 K visibly evolves over time ( $t$  = 0 h corresponds to a measurement directly after thermal annealing at 120 °C). Qualitatively, the same species are present over the whole period, but their relative amount changes, suggesting re-equilibration to the most thermodynamically stable state. This process is likely affected by the presence of weak noncovalent interactions.

To scrutinize the nature of the two TFDIB species observed experimentally for all the modulated samples by <sup>19</sup>F NMR (species 1 at −108 ppm and −119 ppm, and species 2 at −116 ppm), we investigated different binding modes between TFDIB and the  $\alpha$ -FAPbI<sub>3</sub> surface as a model by means of DFT calculations (for more details see Section S2, Figures S3–S11, and Tables S3–S6 in the SI). We compared the experimental <sup>19</sup>F chemical shifts with calculated chemical shifts for different binding modes. We investigated both *symmetric* (S; Figure 1c and Figures S4–S5 in the SI) and *asymmetric* (A) binding modes (Figure 1b and Figure S3, S6 in the SI). Moreover, although higher directionality of XB is expected as compared to HB,<sup>27–29</sup> we also considered the possibility of TFDIB occupying the A-site position on the perovskite surface (in modes Aa and Sa shown in Figure 1b,c). The <sup>19</sup>F chemical shifts were calculated using plane-wave DFT (described in Section S2 of the SI) and compared to the experimental data (summarized in Figure 6).

The calculated <sup>19</sup>F chemical shifts for each of the asymmetric Aa modes are clustered into two distinct groups, separated by around 10–20 ppm (Table S5, SI). These groups correspond, within the expected DFT error, to the experimental <sup>19</sup>F chemical shifts of species 1 (Figure 6). In contrast, the <sup>19</sup>F chemical shifts of the symmetric Sa modes are more spread out (at least three groups per mode) and are shifted to much lower chemical shifts (up to −145 ppm), which are not in agreement with any of the observed <sup>19</sup>F species, excluding the bifunctional A-site binding (i.e., Sa mode) for XB modulators.

Since XB interaction takes place through the  $\sigma$  hole (Figure 2), rendering XB highly directional,<sup>27–29</sup> it is envisaged that the bifunctional XB would be more likely to take place through binding with the iodide anions of the [PbI<sub>6</sub>]<sup>4−</sup> octahedra, corresponding to the Sx mode. To further assess this hypothesis, we generated an ensemble of 270 XB mode structures (details in Section S2 of the SI), and we considered two main halogen binding modes, namely the Sx, where the TFDIB cations are interlocked between two FAPbI<sub>3</sub> surfaces (similar to a “Dion–Jacobson-type” layered perovskite motifs,<sup>10</sup> Sx-DJ or Sx), and Ax, where the XB occurs asymmetrically on the surface of the perovskite with alternating TFDIB cations shifted with respect to one another (resembling “Ruddlesden–Popper-type” layered perovskites;<sup>41</sup>

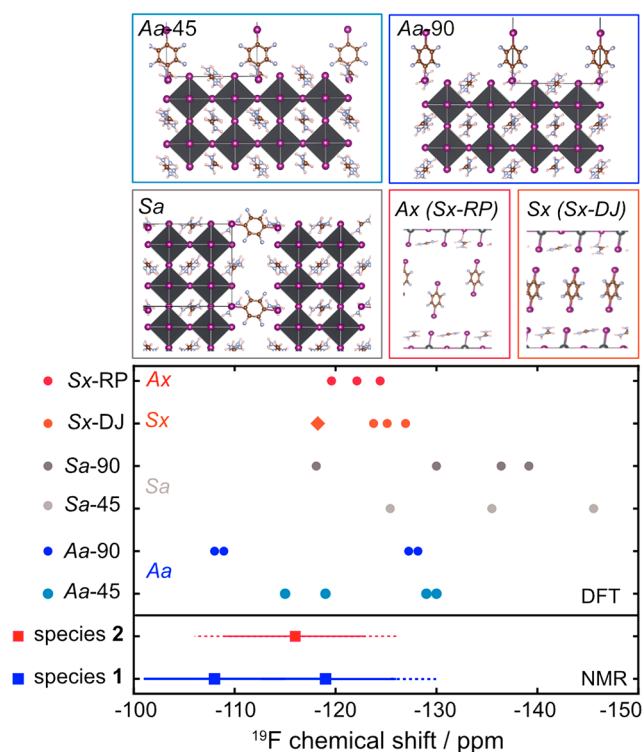


**Figure 6.** DFT calculations of the XB binding modes. Top: Optimized structures of the various binding modes of the TFDIB modulator. Bottom: DFT-calculated <sup>19</sup>F chemical shifts for the investigated modes (Ax, Sx, Sa, and Aa) and experimental <sup>19</sup>F chemical shifts of the species (1 and 2), suggesting absence of the Sa interaction modes. The solid lines (red and blue) indicate the estimated mean deviation between experimental and calculated <sup>19</sup>F chemical shifts of 7 ppm. The dashed lines (red and blue) indicate the approximated maximum error between experimental and calculated <sup>19</sup>F chemical shifts of around 10 ppm. For details see Section S2 in the SI.

Sx-RP or Ax, as detailed in Figure S6 and represented in Figure 6). After DFT optimization that included fully relativistic corrections, we selected an ensemble of 16 halogen binding modes (5 from the Ax and 11 from the Sx modes), for which we calculated <sup>19</sup>F chemical shifts (details in Section S2 of the SI).

The calculated <sup>19</sup>F chemical shifts for both the Sx and the Ax modes (*symmetric* crosslinking, Figures 2b and 6) match, within the expected DFT error, the experimental <sup>19</sup>F chemical shifts. While the Aa species agree more closely with those of species 1, the Sx/Ax align well with the shifts of species 2. The Sx modes are found to be energetically more favorable, and their spread is in better agreement with the experimental values, whereas the absolute positions of the Ax modes are in better agreement with the species 2. Furthermore, the relative positions of the <sup>19</sup>F chemical shifts of the Aa (*asymmetric* surface binding, Figures 2b and 6) and Sx/Ax modes display the same trend as the relative positions of the experimental <sup>19</sup>F chemical shifts of species 1 and 2 (Figure 6), respectively, confirming the assignments. To the best of our knowledge, this finding provides the first atomic-level evidence of a long-hypothesized bifunctional molecular crosslinking in hybrid perovskite materials, in this case via XB. The existence of these species in the XB-modulated perovskites is expected to affect their photovoltaic performance.

### Photovoltaic Performance upon XB Modulation.

Photovoltaic (PV) devices of the n-i-p architecture were fabricated by assembling the constituent layers as described in the **Experimental Details**: FTO/(40 nm) c-TiO<sub>2</sub>/(250 nm) mp-TiO<sub>2</sub>/(450 nm) perovskite/(180 nm) 2,2',7,7'-tetrakis-(*N,N*-di-4-methoxyphenylamino)-9,9'-spirobifluorene (Spiro-OMeTAD)/(80 nm) Au. The thicknesses of the layers were estimated by cross-sectional SEM imaging (**Figure 7a**, inset). The effect of the XB modulator TFDIB on the photovoltaic devices was tested by either adding it directly into the perovskite precursor solution or by casting it as a modulating layer at the interface between the perovskite and the Spiro-OMeTAD (optimization conditions are detailed in the **Experimental Details** and the **Section S3** of the SI). It was found that higher concentrations (50 mM) of the XB modulator inside the precursor solution provides gains in the open circuit voltage ( $V_{OC}$ ; **Figures S12–S13**, SI). However, the fill factor (FF) and the short circuit current density ( $J_{SC}$ ) are adversely affected, resulting in lower efficiency as compared to control cells without the XB modulator. In contrast, when applying lower concentrations (10 mM), a gain in  $V_{OC}$  is achieved without compromising the  $J_{SC}$ , with a minor effect on the FF, resulting in efficiencies slightly lower than those of control devices (**Figure S13**, SI). The performances were, however, superior when the XB modulator was applied as an interlayer (**Figures S14–S15**, SI).

Different concentrations in the interlayer precursor solution (5–50 mM) were tested to define the conditions that result in devices with the best characteristics (**Figures S14–S20**, SI). It was found that, for concentrations below 50 mM, varying the concentration of the XB modulator has little effect on the conversion efficiency of the devices and that XB modulator concentration of 10 mM results in higher power conversion efficiencies (PCE > 20%) with better overall reproducibility. Thereby, the study focuses on devices with the XB modulator as an interlayer (**Figures S14–S16**, SI). The average PV metrics display values of  $J_{SC} = 24.4 \text{ mA cm}^{-2}$ ,  $V_{OC} = 1.07 \text{ V}$ , FF = 0.78, and PCE = 20.4% for pristine and  $J_{SC} = 24.4 \text{ mA cm}^{-2}$ ,

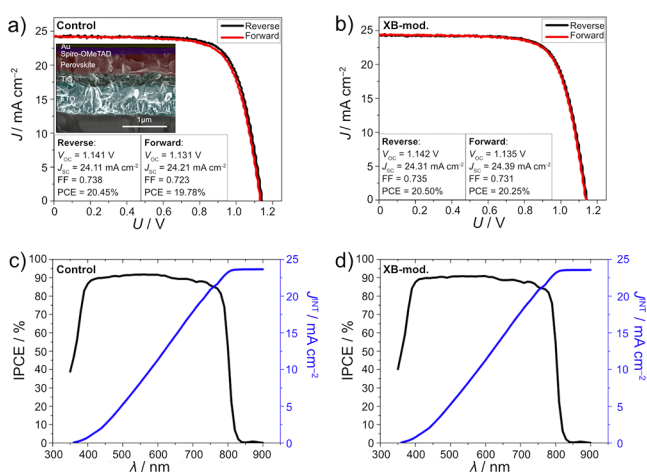


**Figure 7.** Photovoltaic performance of perovskite solar cells.  $J$ - $V$  curves of representative (a) control and (b) XB-modulated (mod.) devices in reverse and forward bias with the PV metrics. The cross-sectional SEM image of the device is shown in the inset in (a). IPCE spectrum of the champion (c) control and (d) XB-modulated (mod.) devices with the projected photocurrents (in blue) derived from integrating the IPCE over the spectral emission.

$V_{OC} = 1.08 \text{ V}$ , FF = 0.78 and PCE = 20.6% for XB-modulated devices (**Figure 7a–d**; champion cells are shown in **Figure S16** of the SI with PV device statistics shown in **Figure 8a–d**). The current densities of  $23.6 \text{ mA cm}^{-2}$  derived by integrating the incident-photon-conversion-efficiency (IPCE) spectra ( $J_{INT}^{INT}$ ) were in good agreement with the values obtained from the  $J$ - $V$  curves (**Figure 7c,d**), which excludes any significant spectral mismatch between the simulator and AM 1.5G solar source. Hysteresis in the XB-modulated cells is only found to be slightly affected.

The long-term operational stability measurements of the modulated devices highlight their superior performances as compared to those using the pristine perovskite (**Figure 8e** and **Figure S18**, SI). The improvement is particularly evident for the devices employing XB-modulated interlayers. Evolution of the maximum power point (MPP) under continuous illumination under nitrogen at room temperature for 500 h shows that the XB-modulated devices retain more than 80% of their initial efficiency, while the control devices retain only about 70% (**Figure 8e**). The possible role of the modulator in affecting the ion migration could be relevant for long-term operational stability.

Halogen bonding to the halide ions, as well as the capacity of fluoroarene moieties to bind halide ions via  $\pi$ -anion interactions,<sup>42</sup> was assumed to result in the changes in the ion migration. We have probed ion migration upon insertion of the modulator by conducting temperature-dependent transient

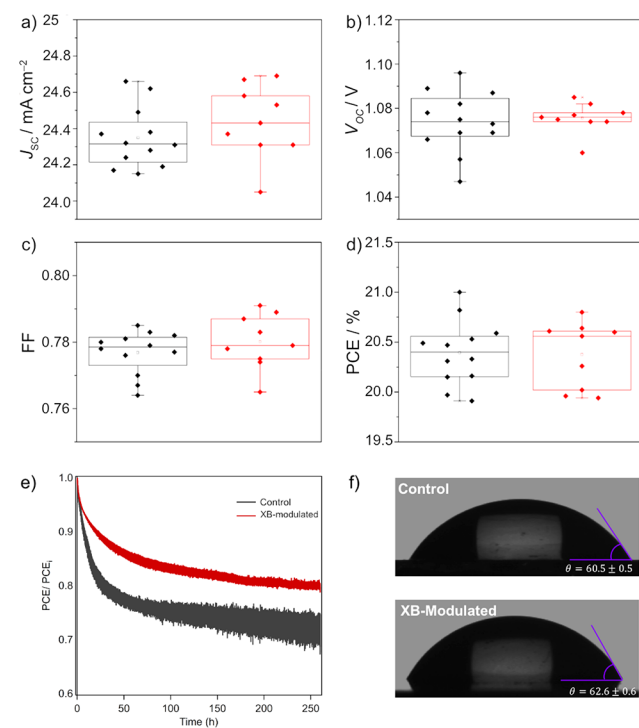


**Figure 8.** Performance of XB-modulated perovskite solar cells. (a–d) PCE statistics based on 21 solar cells.  $J$ - $V$  curves are recorded at a scanning rate of  $50 \text{ mV s}^{-1}$  under standard AM 1.5G solar radiation and reverse bias (from  $V_{OC}$  to  $J_{SC}$ ) of pristine (control, black) and XB-modulated (red) devices. (e) Evolution of the PCE based on maximum power point (MPP) tracking of unsealed PSCs with aperture area of  $0.16 \text{ cm}^2$  using pristine (black) and XB (red) perovskite films under continuous illumination under nitrogen at ambient temperature. (f) Contact angle measurements with the water droplet of the pristine (control) and XB-modulated perovskite films.

capacitance measurements on pristine and modulated perovskite solar cells to establish whether the presence of the modulator results in changes of the halide mobility in the corresponding devices (details are provided in Section S4, SI).<sup>23</sup> The transient ion drift measurements at variable temperatures suggest two mobile anion species with activation energies of 0.12 and 0.10 eV and diffusion coefficients of  $3.6 \times 10^{-12}$  and  $2.0 \times 10^{-11} \text{ cm}^2 \text{ s}^{-1}$  for the pristine samples (Figures S21–S23 and Tables S7–S8, SI). Upon modulation, both the activation energies and the diffusion coefficients remain comparable, indicating that the effect of the modulation is not primarily related to ion migration under these experimental conditions. We thereby assume that this is more likely to result from the relative stabilization of the  $\alpha$ -FAPbI<sub>3</sub> phase, as suggested by the XRD analysis. Furthermore, the hydrophobic nature of the modulator is important for protecting the perovskite from moisture and oxygen exposure, among other degrading factors.<sup>43–45</sup> The contact angle measurements of XB-modulated films show a minor increase compared to those of the pristine ones (Figure 8f), presumably as a result of employing small concentrations of the modulator in conjunction with a highly hydrophobic antisolvent. The resulting operational stability enhancement without compromising the performance highlights the potential of supramolecular modulation via weak noncovalent interactions such as XB for solar cell advancement.

## CONCLUSION

In summary, we have shown the potential of bifunctional halogen bonding to modulate the properties of hybrid lead halide perovskites by employing 1,2,4,5-tetrafluoro-3,6-diiodobenzene (TFDIB). We have evaluated the atomic-level mode of interaction of TFDIB with perovskites by solid-state NMR spectroscopy in conjunction with DFT calculations, evidencing crosslinking via halogen bonding. By adding the modulator to perovskite formulations, we obtain highly efficient solar cells with solar-to-electric power conversion efficiencies exceeding 20%. Moreover, supramolecular modulation via halogen bonding leads to enhanced stability under continuous illumination without compromising the resulting photovoltaic performance. This emphasizes the potential of approaches exploiting halogen bonding in hybrid perovskite-based photovoltaics.

## ASSOCIATED CONTENT

### Supporting Information

The Supporting Information is available free of charge at <https://pubs.acs.org/doi/10.1021/jacs.9b13701>.

Materials and methods, DFT energy and NMR chemical shift calculations, supplementary data, and transient capacitance measurements (PDF)

DFT calculations: A-site binding mode (ZIP)

DFT calculations: Competing interactions (ZIP)

DFT calculations: Halogen binding mode (ZIP)

DFT calculations: Reference structures (ZIP)

## AUTHOR INFORMATION

### Corresponding Authors

\*E-mail: [lyndon.emsley@epfl.ch](mailto:lyndon.emsley@epfl.ch) (L.E.).

\*E-mail: [jovana.milic@epfl.ch](mailto:jovana.milic@epfl.ch) (J.V.M.).

\*E-mail: [michael.gratzel@epfl.ch](mailto:michael.gratzel@epfl.ch) (M.G.).

## ORCID

Dominik J. Kubicki: 0000-0002-9231-6779

Moritz H. Futscher: 0000-0001-8451-5009

Amita Ummadisingu: 0000-0002-5851-4827

Renana Gershoni-Poranne: 0000-0002-2233-6854

Lyndon Emsley: 0000-0003-1360-2572

Jovana V. Milić: 0000-0002-9965-3460

Michael Grätzel: 0000-0002-0068-0195

## Present Address

<sup>∇</sup>Cavendish Laboratory, University of Cambridge, J. J. Thomson Avenue, Cambridge CB3 0HE, United Kingdom.

## Author Contributions

<sup>#</sup>These authors contributed equally to this work.

## Notes

The authors declare no competing financial interest.

## ACKNOWLEDGMENTS

J.V.M., S.M.Z., and M.G. are grateful to the European Union's Horizon 2020 research and innovation program under grant agreement no. 826013 (IMPRESSIVE) as well as the GRAPHENE Flagship Core 2 project supported by the European Commission H2020 Programme under contract 785219. D.J.K., A.H., and L.E. acknowledge support from Swiss National Science Foundation grant no. 200020\_178860. M.A.R.P. is grateful to CONACyT/SENER Mexico for the financial support granted through the project 291195. The work of L.M., M.H.F., and B.E. is part of the Dutch Research Council (NWO) and was performed at the research institute AMOLF. Authors are grateful to Dr. Yang Li (formerly based at EPFL, presently at Karlsruhe Institute of Technology) for his support in processing the stability measurement data, Anand Agarwalla (EPFL) for support in performing the stability studies, Dr. Ji-Youn Seo (EPFL) for support with the cross-sectional SEM measurements, and Dr. Anatol Schwaab (ETH Zurich) for insightful discussions and valuable support concerning the electrostatic potential surface mapping representations.

## REFERENCES

- (1) Zhang, H.; Nazeeruddin, M. K.; Choy, W. C. H. Perovskite Photovoltaics: The Significant Role of Ligands in Film Formation, Passivation, and Stability. *Adv. Mater.* **2019**, *31*, 1805702.
- (2) Grätzel, M. The Light and Shade of Perovskite Solar Cells. *Nat. Mater.* **2014**, *13*, 838–842.
- (3) NREL Best Research Cell Efficiency Chart; <https://www.nrel.gov/pv/assets/pdfs/best-research-cell-efficiencies.20190802.pdf> (accessed August 2019).
- (4) Rong, Y.; Hu, Y.; Mei, A.; Tan, H.; Saidaminov, M. I.; Seok, S. I.; McGehee, M. D.; Sargent, E. H.; Han, H. Challenges for Commercializing Perovskite Solar Cells. *Science* **2018**, *361*, No. eaat8235.
- (5) (a) Cho, K. T.; Zhang, Y.; Orlandi, S.; Cavazzini, M.; Zimmermann, I.; Lesch, A.; Tabet, N.; Pozzi, G.; Grancini, G.; Nazeeruddin, M. K. Water-Repellent Low-Dimensional Fluorous Perovskite as Interfacial Coating for 20% Efficient Solar Cells. *Nano Lett.* **2018**, *18*, 5467–5474. (b) Liu, Y.; Akin, S.; Pan, L.; Uchida, R.; Arora, N.; Milić, J. V.; Hinderhofer, A.; Schreiber, F.; Uhl, A. R.; Zakeeruddin, S. M.; Hagfeldt, A.; Dar, M. I.; Grätzel, M. Ultrahydrophobic 3D/2D Fluoroarene Bilayer-Based Water-Resistant Perovskite Solar Cells with Efficiencies Exceeding 22%. *Sci. Adv.* **2019**, *5*, No. eaaw2543.
- (6) Milić, J. V.; Arora, N.; Dar, M. I.; Zakeeruddin, S. M.; Grätzel, M. Reduced Graphene Oxide as a Stabilizing Agent in Perovskite Solar Cells. *Adv. Mater. Interfaces* **2018**, *5*, 1800416.

- (7) Milić, J. V.; Kubicki, D. J.; Emsley, L.; Grätzel, M. Multifunctional Molecular Modulation for Efficient and Stable Hybrid Perovskite Solar Cells. *Chimia* **2019**, *73*, 317–323.
- (8) Guo, P.; Ye, Q.; Yang, X.; Zhang, J.; Xu, F.; Shchukin, D.; Wei, B.; Wang, H. Surface & Grain Boundary Co-Passivation by Fluorocarbon Based Bifunctional Molecules for Perovskite Solar Cells with Efficiency over 21%. *J. Mater. Chem. A* **2019**, *7*, 2497–2506.
- (9) Li, X.; Dar, M. I.; Yi, C.; Luo, J.; Tschumi, M.; Zakeeruddin, S. M.; Nazeeruddin, M. K.; Han, H.; Grätzel, M. Improved Performance and Stability of Perovskite Solar Cells by Crystal Crosslinking with Alkylphosphonic Acid  $\omega$ -Ammonium Chlorides. *Nat. Chem.* **2015**, *7*, 703–711.
- (10) Mao, L.; Stoumpos, C. C.; Kanatzidis, M. G. Two-Dimensional Hybrid Halide Perovskites: Principles and Promises. *J. Am. Chem. Soc.* **2019**, *141*, 1171–1190.
- (11) (a) Li, Y.; Milić, J. V.; Ummadisingu, A.; Seo, J.-Y.; Im, J.-H.; Kim, H.-S.; Liu, Y.; Dar, M. I.; Zakeeruddin, S. M.; Wang, P.; Hagfeldt, A.; Grätzel, M. Bifunctional Organic Spacers for Formamidinium-Based Hybrid Dion-Jacobson Two-Dimensional Perovskite Solar Cells. *Nano Lett.* **2019**, *19*, 150–157. (b) Milić, J. V.; Im, J.-H.; Kubicki, D. J.; Ummadisingu, A.; Seo, J.-Y.; Li, Y.; Ruiz Preciado, M. A.; Dar, M. I.; Zakeeruddin, S. M.; Emsley, L.; Grätzel, M. Supramolecular Engineering for Formamidinium-Based Layered 2D Perovskite Solar Cells: Structural Complexity and Dynamics Revealed by Solid-State NMR Spectroscopy. *Adv. Energy Mater.* **2019**, *9*, 1900284.
- (12) Ke, W.; Mao, L.; Stoumpos, C. C.; Hoffman, J.; Spanopoulos, I.; Mohite, A. D.; Kanatzidis, M. G. Compositional and Solvent Engineering in Dion–Jacobson 2D Perovskites Boosts Solar Cell Efficiency and Stability. *Adv. Energy Mater.* **2019**, *9*, 1803384.
- (13) Abate, A.; Saliba, M.; Hollman, D. J.; Stranks, S. D.; Wojciechowski, K.; Avolio, R.; Grancini, G.; Petrozza, A.; Snaith, H. J. Supramolecular Halogen Bond Passivation of Organic-Inorganic Halide Perovskite Solar Cells. *Nano Lett.* **2014**, *14*, 3247–3254.
- (14) Bi, S.; Wang, H.; Zhou, J.; You, S.; Zhang, Y.; Shi, X.; Tang, Z.; Zhou, H. J. Halogen Bonding Reduces Intrinsic Traps and Enhances Charge Mobilities in Halide Perovskite Solar Cells. *J. Mater. Chem. A* **2019**, *7*, 6840–6848.
- (15) Erdélyi, M. Halogen Bonding in Solution. *Chem. Soc. Rev.* **2012**, *41*, 3547–3557.
- (16) He, W.; Ge, Y.-C.; Tan, C.-H. Halogen-Bonding-Induced Hydrogen Transfer to C = N Bond with Hantzsch Ester. *Org. Lett.* **2014**, *16*, 3244–3247.
- (17) Gilday, L. C.; Robinson, S. W.; Barendt, T. A.; Langton, M. J.; Mullaney, B. R.; Beer, P. D. Halogen Bonding in Supramolecular Chemistry. *Chem. Rev.* **2015**, *115*, 7118–7195.
- (18) Simon, S. J. C.; Parlange, F. G. L.; Swords, W. B.; Kellett, C. W.; Du, C.; Lam, B.; Dean, R. K.; Hu, K.; Meyer, G. J.; Berlinguette, C. P. Halogen Bonding Promotes Higher Dye-Sensitized Solar Cell Photovoltages. *J. Am. Chem. Soc.* **2016**, *138*, 10406–10409.
- (19) (a) Bi, D.; Li, X.; Milić, J. V.; Kubicki, D. J.; Pellet, N.; Luo, J.; LaGrange, T.; Mettraux, P.; Emsley, L.; Zakeeruddin, S. M.; Grätzel, M. Multifunctional Molecular Modulators for Perovskite Solar Cells with Over 20% Efficiency and High Operational Stability. *Nat. Commun.* **2018**, *9*, 4482. (b) Alharbi, E. A.; Alyamani, A. Y.; Kubicki, D. J.; Uhl, A. R.; Walder, B. J.; Alanazi, A. Q.; Luo, J.; Burgos-Caminal, A.; Albadri, A.; Albrithen, H.; Alotaibi, M. H.; Moser, J.-E.; Zakeeruddin, S. M.; Giordano, F.; Emsley, L.; Grätzel, M. Atomic-Level Passivation Mechanism of Ammonium Salts Enabling Highly Efficient Perovskite Solar Cells. *Nat. Commun.* **2019**, *10*, 3008.
- (20) Prochowicz, D.; Franckevičius, M.; Cieślak, A. M.; Zakeeruddin, S. M.; Grätzel, M.; Lewiński, J. Mechanosynthesis of the Hybrid Perovskite  $\text{CH}_3\text{NH}_3\text{PbI}_3$ : Characterization and the Corresponding Solar Cell Efficiency. *J. Mater. Chem. A* **2015**, *3*, 20772–20777.
- (21) Prochowicz, D.; Yadav, P.; Saliba, M.; Sasaki, M.; Zakeeruddin, S. M.; Lewiński, J.; Grätzel, M. Mechanosynthesis of Pure Phase Mixed-Cation  $\text{MA}_x\text{FA}_{1-x}\text{PbI}_3$  Hybrid Perovskites: Photovoltaic Performance and Electrochemical Properties. *Sustain. Energy Fuels* **2017**, *1*, 689–693.
- (22) Rosales, B. A.; Wei, L.; Vela, J. Synthesis and Mixing of Complex Halide Perovskites by Solvent-Free Solid-State Methods. *J. Solid State Chem.* **2019**, *271*, 206–215.
- (23) Futscher, M. H.; Lee, J. M.; McGovern, L.; Muscarella, L. A.; Wang, T.; Haider, M. I.; Fakharuddin, A.; Schmidt-Mende, L.; Ehrler, B. Quantification of Ion Migration in  $\text{CH}_3\text{NH}_3\text{PbI}_3$  Perovskite Solar Cells by Transient Capacitance. *Mater. Horiz.* **2019**, *6*, 1497–1503.
- (24) (a) Foresman, J. B.; Frisch, A. E. *Exploring Chemistry with Electronic Structure Methods*, 2nd ed.; Gaussian, Inc.: Wallingford, CT, 1995; pp 1–335. (b) Frisch, M. J.; Trucks, G. W.; Schlegel, H. B.; Scuseria, G. E.; Robb, M. A.; Cheeseman, J. R.; Scalmani, G.; Barone, V.; Petersson, G. A.; Nakatsuji, H.; Li, X.; Caricato, M.; Marenich, A. V.; Bloino, J.; Janesko, B. G.; Gomperts, R.; Mennucci, B.; Hratchian, H. P.; Ortiz, J. V.; Izmaylov, A. F.; Sonnenberg, J. L.; Williams-Young, D.; Ding, F.; Lipparini, F.; Egidi, F.; Goings, J.; Peng, B.; Petrone, A.; Henderson, T.; Ranasinghe, D.; Zakrzewski, V. G.; Gao, J.; Rega, N.; Zheng, G.; Liang, W.; Hada, M.; Ehara, M.; Toyota, K.; Fukuda, R.; Hasegawa, J.; Ishida, M.; Nakajima, T.; Honda, Y.; Kitao, O.; Nakai, H.; Vreven, T.; Throssell, K.; Montgomery, J. A., Jr; Peralta, J. E.; Ogliaro, F.; Bearpark, M. J.; Heyd, J. J.; Brothers, E. N.; Kudin, K. N.; Staroverov, V. N.; Keith, T. A.; Kobayashi, R.; Normand, J.; Raghavachari, K.; Rendell, A. P.; Burant, J. C.; Iyengar, S. S.; Tomasi, J.; Cossi, M.; Millam, J. M.; Klene, M.; Adamo, C.; Cammi, R.; Ochterski, J. W.; Martin, R. L.; Morokuma, K.; Farkas, O.; Foresman, J. B.; Fox, D. J. *Gaussian 16*, Revision A.03; Gaussian, Inc.: Wallingford, CT, 2016.
- (25) (a) Hu, Y.; Schlipf, J.; Wussler, M.; Petrus, M. L.; Jaegermann, W.; Bein, T.; Müller-Buschbaum, P.; Docampo, P. Hybrid Perovskite/Perovskite Heterojunction Solar Cells. *ACS Nano* **2016**, *10*, 5999–6007. (b) Kanno, S.; Imamura, Y.; Hada, M. First-Principles Calculations of the Rotational Motion and Hydrogen Bond Capability of Large Organic Cations in Hybrid Perovskites. *J. Phys. Chem. C* **2018**, *122*, 15966–15972.
- (26) Tavakoli, M. M.; Tress, W.; Milić, J. V.; Kubicki, D.; Emsley, L.; Grätzel, M. Addition of Adamantylammonium Iodide to Hole Transport Layers Enables Highly Efficient and Electroluminescent Perovskite Solar Cells. *Energy Environ. Sci.* **2018**, *11*, 3310–3320.
- (27) Clark, T.; Hennemann, M.; Murray, J. S.; Politzer, P. Halogen Bonding: The  $\sigma$ -Hole. *J. Mol. Model.* **2007**, *13*, 291–296.
- (28) Wang, H.; Wang, W.; Jin, W. J.  $\sigma$ -Hole Bond vs  $\pi$ -Hole Bond: A Comparison Based on Halogen Bond. *Chem. Rev.* **2016**, *116*, S072–S104.
- (29) Kolář, M. H.; Hobza, P. Computer Modeling of Halogen Bonds and Other  $\sigma$ -Hole Interactions. *Chem. Rev.* **2016**, *116*, S155–S187.
- (30) (a) Xiao, M.; Huang, F.; Huang, W.; Dkhissi, Y.; Zhu, Y.; Etheridge, J.; Gray-Weale, A.; Bach, U.; Cheng, Y.-B.; Spiccia, L. A Fast Deposition-Crystallization Procedure for Highly Efficient Lead Iodide Perovskite Thin-Film Solar Cells. *Angew. Chem., Int. Ed.* **2014**, *53*, 9898–9903. (b) Paek, S.; Schouwink, P.; Athanasopoulou, E. N.; Cho, K. T.; Grancini, G.; Lee, Y.; Zhang, Y.; Stellacci, F.; Nazeeruddin, M. K.; Gao, P. From Nano- to Micrometer Scale: The Role of Antisolvent Treatment on High Performance Perovskite Solar Cells. *Chem. Mater.* **2017**, *29*, 3490–3498.
- (31) Noel, N. K.; Habisreutinger, S. N.; Wenger, B.; Klug, M. T.; Hörantner, M. T.; Johnston, M. B.; Nicholas, R. J.; Moore, D. T.; Snaith, H. J. A Low Viscosity, Low Boiling Point, Clean Solvent System for the Rapid Crystallisation of Highly Specular Perovskite Films. *Energy Environ. Sci.* **2017**, *10*, 145–152.
- (32) Levine, I.; Hodes, G.; Snaith, H. J.; Nayak, P. K. How to Avoid Artifacts in Surface Photovoltage Measurements: A Case Study with Halide Perovskites. *J. Phys. Chem. Lett.* **2017**, *8*, 2941–2943.
- (33) (a) deQuilettes, D. W.; Vorpahl, S. M.; Stranks, S. D.; Nagaoka, H.; Eperon, G. E.; Ziffer, M. E.; Snaith, H. J.; Ginger, D. S. Impact of Microstructure on Local Carrier Lifetime in Perovskite Solar Cells. *Science* **2015**, *348*, 683–686. (b) deQuilettes, D. W.; Koch, S.; Burke, S.; Paranj, R. K.; Shropshire, A. J.; Ziffer, M. E.; Ginger, D. S. Photoluminescence Lifetimes Exceeding 8  $\mu\text{s}$  and Quantum Yields

Exceeding 30% in Hybrid Perovskite Thin Films by Ligand Passivation. *ACS Energy Lett.* **2016**, *1*, 438–444.

(34) Lindsey, C. P.; Patterson, G. D. Detailed Comparison of the Williams–Watts and Cole–Davidson Functions. *J. Chem. Phys.* **1980**, *73*, 3348–3357.

(35) Kubicki, D. J.; Prochowicz, D.; Hofstetter, A.; Péchy, P.; Zakeeruddin, S. M.; Grätzel, M.; Emsley, L. Cation Dynamics in Mixed-Cation(MA)<sub>x</sub>(FA)<sub>1-x</sub>PbI<sub>3</sub> Hybrid Perovskites from Solid-State NMR. *J. Am. Chem. Soc.* **2017**, *139*, 10055–10061.

(36) Kubicki, D. J.; Prochowicz, D.; Hofstetter, A.; Zakeeruddin, S. M.; Grätzel, M.; Emsley, L. Phase Segregation in Cs-, Rb- and K-Doped Mixed-Cation (MA)<sub>x</sub>(FA)<sub>1-x</sub>PbI<sub>3</sub> Hybrid Perovskites from Solid-State NMR. *J. Am. Chem. Soc.* **2017**, *139*, 14173–14180.

(37) Kubicki, D. J.; Prochowicz, D.; Hofstetter, A.; Sasaki, M.; Yadav, P.; Bi, D.; Pellet, N.; Lewiński, J.; Zakeeruddin, S. M.; Grätzel, M.; Emsley, L. Formation of Stable Mixed Guanidinium-Methylammonium Phases with Exceptionally Long Carrier Lifetimes for High-Efficiency Lead Iodide-Based Perovskite Photovoltaics. *J. Am. Chem. Soc.* **2018**, *140*, 3345–3351.

(38) Kubicki, D. J.; Prochowicz, D.; Hofstetter, A.; Zakeeruddin, S. M.; Grätzel, M.; Emsley, L. Phase Segregation in Potassium-Doped Lead Halide Perovskites from <sup>39</sup>K Solid-State NMR at 21.1 T. *J. Am. Chem. Soc.* **2018**, *140*, 7232–7238.

(39) Szell, P. M. J.; Gabriel, S. A.; Gill, R. D. D.; Wan, S. Y. H.; Gabidullin, B.; Bryce, D. L. <sup>13</sup>C and <sup>19</sup>F solid-state NMR and X-ray Crystallographic Study of Halogen-Bonded Frameworks Featuring Nitrogen-Containing Heterocycles. *Acta Crystallogr., Sect. C: Struct. Chem.* **2017**, *C73*, 157–167.

(40) Abragam, A. *Principles of Nuclear Magnetism*; Oxford University Press: New York, 1961.

(41) Stoumpos, C. C.; Cao, D. H.; Clark, D. J.; Young, J.; Rondinelli, J. M.; Jang, J. I.; Hupp, J. T.; Kanatzidis, M. G. Ruddlesden-Popper Hybrid Lead Iodide Perovskite 2D Homologous Semiconductors. *Chem. Mater.* **2016**, *28*, 2852–2867.

(42) Giese, M.; Albrecht, M.; Rissanen, K. Anion- $\pi$  Interactions with Fluoroarenes. *Chem. Rev.* **2015**, *115*, 8867–8895.

(43) Domanski, K.; Roose, B.; Matsui, T.; Saliba, M.; Turren-Cruz, S.-H.; Correa-Baena, J.-P.; Carmona, C. R.; Richardson, G.; Foster, J. M.; De Angelis, F.; Ball, J. M.; Petrozza, A.; Mine, N.; Nazeeruddin, M. K.; Tress, W.; Grätzel, M.; Steiner, U.; Hagfeldt, A.; Abate, A. Migration of Cations Induces Reversible Performance Losses Over Day/Night Cycling in Perovskite Solar Cells. *Energy Environ. Sci.* **2017**, *10*, 604–613.

(44) Domanski, K.; Correa-Baena, J.-P.; Mine, N.; Nazeeruddin, M. K.; Abate, A.; Saliba, M.; Tress, W.; Hagfeldt, A.; Grätzel, M. Not All That Glitters Is Gold: Metal-Migration-Induced Degradation in Perovskite Solar Cells. *ACS Nano* **2016**, *10*, 6306–6314.

(45) Domanski, K.; Alharbi, E. A.; Hagfeldt, A.; Grätzel, M.; Tress, W. Systematic Investigation of the Impact of Operation Conditions on the Degradation Behaviour of Perovskite Solar Cells. *Nat. Energy* **2018**, *3*, 61–67.